Axisymmetric Predictions of Fluid Flow inside a Rotating Cavity System

MUJEEBUDDIN MEMON*, ABDUL FATAH ABBASI**, AND JAWAID DAUDPOTO**

RECEIVED ON 27.11.2012 ACCEPTED ON 20.03.2013

ABSTRACT

Accurate prediction of fluid flow in the rotating cavity system is of practical interest as it is most commonly used in the gas turbine engines and compressors. This paper presents the numerical predictions of a rotating cavity flow system for Reynolds numbers of the range $1x10^5 \leq Re_\theta \leq 4x10^5$ and two different mass flow rates C_w=1092 and 2184. A finite-difference technique is employed for a Steady-state solution in the axisymmetric cylindrical polar coordinate frame of reference. The two low Reynolds number turbulence models, the low Reynolds number k-ε model and the low Reynolds number second moment closure have been used to compute the basic characteristics of the flow inside the rotating cavity flow system. Different flow regions have been identified by computing flow structures and dimensions of those regions have also been studied under different flow rates. A comparison of the computed variation of moment coefficient of both the turbulence models are presented for the above mentioned parameters and the parametric effects on the moment coefficients have been discussed.

Key Words: **Rotating Cavity Flow System, Reynolds Number, Finite Difference Method, Axisymmetric Cylindrical Polar Coordinate Frame of Reference.**

1. INTRODUCTION

The knowledge of the internal air cooling system of the gas turbine engines is essential for the turbo-machinery designers and engineers, to estimate the correct amount of cooling air, which bleeds from the intermediate stage of the compressor at the cost of fuel consumption. Childs, et. al. [1] mentioned that about 20% of the engine core flow is extracted from the compressor for the engine cooling purpose at the cost of 5% of fuel consumption. Therefore, it is essential to optimise the use of cooling air and enhance the turbine cycle efficiency of the engine. The significance of this problem has inspired many researchers to devote their efforts in this field. Since last four decades, many researchers have conducted the experimental, numerical and theoretical studies. Previous studies mentioned that at constant temperature heating, the flow structure inside the cavity is analogous to the isothermal flow structure, whereas, in the asymmetrical heating, the flow structure is

* Professor, and **Assistant Professor,
Department of Mechanical Engineering, Mehran University of Engineering & Technology, Jamshoro.

altered by the rotationally-induced buoyancy effects. These effects were illustrated in the work of Owen, et. al. [2,3] and Schiestel, et. al. [4] . Owen and Rogers [5] presented a comprehensive review of flow and heat transfer in rotating cavities. Gan, et. al. [6], Soong, et. al. [7] and Randriamampianina, et. al. [8] carried out the experimental and numerical studies for these systems. Recently, Poncet, et. al. [9] presented investigations for rotating cavity flows according to geometrical configurations of Owen and Pincombe [10] at lower rotational Reynolds number Re_θ of $1x10^5$. These investigations were carried out by adopting the eddy viscosity RANS (Reynolds Averaged Navier Stokes) and Reynolds stress models within commercially available Fluent and CFX software. They reported that the Reynolds stress model showed the best agreement against the experimental data of Owen and Pincombe [10] particularly for tangential velocity distribution. In present work, fluid flow behaviour in the rotating cavity system has been investigated for varying rotational Reynolds number in the range of $1x10^5 \leq Re_\theta \leq 4x10^5$ and for two mass flow rates, C_w=1092 and 2184 by using two turbulence models, the low Reynolds number k-ε model and the low Reynolds number second moment closure. These models have been chosen because of robustness of their applicability over wide variety of situations. Furthermore simulated results obtained through these models are compared with the experimental data of Pincomb [11]. Previous studies revealed that at varying rotational speeds and fixed mass flow rate, the nature of the flow structure between the co-rotating discs becomes oscillating and chaotic. Therefore, it is need of the hour to understand the fluid flow behaviour in the rotating cavity system, particularly in the source and Ekman layer regions.

This paper is structured as follows: Section 2 presents the problem specification and boundary conditions, Section 3 provides the details about two turbulence models, Section 4 presents the computational procedure, discussion of results are presented in Section 5 and Section 6 presents the conclusions.

2. PROBLEM SPECIFICATION AND BOUNDARY CONDITIONS

The simplified geometrical configuration of rotating cavity system with the radial outflow is presented in Fig. 1. The geometric dimensions and boundary conditions considered here are the same used in the relevant experimental work of Pincombe [11]. The geometrical dimensions and boundary conditions are:

b=0.4425m s=0.059m, and r_i=0.04425m.

where, b, s and r_i are outer radius of cavity, axial gap between discs and inner disc radius respectively.

Boundary conditions are given as under

$U=V=W=0$ at $z=0$, $r_i<r<b$

$V=W=0, U=U_i$ at $z=0$, $0<r<r_i$

$U=V=0, W=\Omega r$ at $z=s$, $0<r<b$

$U=W=0, V=V_o$ at $r=b$, $0<z<S_c$

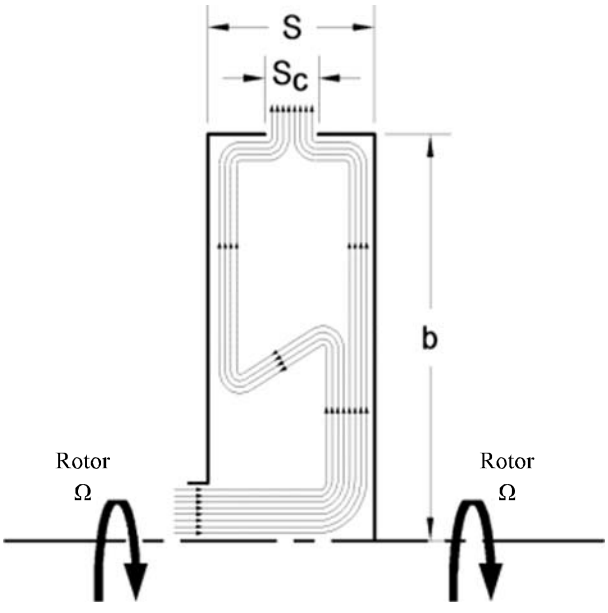

FIG 1. SCHEMATIC DIAGRAM FOR ROTATING CAVITY SYSTEM WITH RADIAL OUT FLOW

3. TURBULENCE MODELS

Turbulence models can be classified into two categories according to their approach for modelling the Reynolds stresses which appear in the time-averaged Navier-Stokes equations. Models that calculate these turbulent stresses with the assumption of an isotropic eddy viscosity approach are labelled as mean-flow closures. In the second category, the assumption of an isotropic eddy viscosity is not invoked and the transport equations for each Reynolds stress component are solved, the so-called Reynolds stress closures. Both models can be further classified into two categories on the basis of their modelling to resolve the flow in the near-wall region where viscous effects are dominant and the turbulence Reynolds number becomes low. The models which resolve this region with the incorporation of wall functions approach to describe the flow between the first grid point and the wall are called high Reynolds number turbulence models. In this kind of approach, the boundary conditions are replaced by matching the conditions to the universality of the law of the wall and local equilibrium of the turbulence. In contrast, the turbulence models which satisfy the physical requirements of the near-wall region as well as the fully turbulent region, are called low Reynolds number turbulence models. Here, additional damping functions have been used to reduce the turbulent transport in the near-wall region and the boundary conditions being imposed at the wall. The details of these models are described in subsections.

3.1 Low Reynolds Number k-ε Model

In the first approach, a well known two equation mean flow closure (low Reynolds number k-ε model) of Morse [12] has been adopted. This model solves the turbulence quantities through the gradient transport hypothesis of Jones and Launder [13-14] which is based on the transport equation for the kinetic energy (k) and its dissipation rate (ε).

$$\overline{\rho u_i u_j} = 2/3\delta_{ij}\,\rho k - \mu_T\left(\frac{\partial U_i}{\partial x_j}+\frac{\partial U_j}{\partial x_i}-2/3\,\delta_{ij}\nabla.\underline{V}\right) \tag{1}$$

where is the divergence of the velocity vector

$$\nabla.\underline{V} = \frac{\partial U}{\partial z}+\frac{\partial V}{\partial r}+\frac{V}{r} \tag{2}$$

= Normal stresses (i.e. i=j only)

These equations can be expressed through the general form:

$$\frac{\partial}{\partial z}(\rho U k)+\frac{1}{r}\frac{\partial}{\partial r}(r\rho V k)=\frac{\partial}{\partial z}\left[\left(\mu+\frac{\mu_T}{\sigma_k}\right)\frac{\partial k}{\partial z}\right]+ \frac{1}{r}\frac{\partial}{\partial r}\left[r\left(\mu+\frac{\mu_T}{\sigma_k}\right)\frac{\partial k}{\partial r}\right]+S_k \tag{3}$$

$$\frac{\partial}{\partial z}(\rho U \varepsilon)+\frac{1}{r}\frac{\partial}{\partial r}(r\rho V \varepsilon)=\frac{\partial}{\partial z}\left[\left(\mu+\frac{\mu_T}{\sigma_\varepsilon}\right)\frac{\partial \varepsilon}{\partial z}\right] +\frac{1}{r}\frac{\partial}{\partial r}\left[r\left(\mu+\frac{\mu_T}{\sigma_\varepsilon}\right)\frac{\partial \varepsilon}{\partial r}\right]+S_\varepsilon \tag{4}$$

where the source terms S_k and S_ε may be given as:

$$S_k = P_k - \rho\varepsilon - D \tag{5}$$

$$S_\varepsilon = c_{\varepsilon 1} f_1 \frac{\varepsilon}{k} P_k - \rho c_{\varepsilon 2} f_2 \frac{\varepsilon^2}{k} + E - F \tag{6}$$

The terms D, E and F represent the near-wall dissipation, the exact dissipation rate in the buffer region and sink term balancing the viscous diffusion at a wall respectively. For full details of these terms, refere Morse, [12].

3.2 Low Reynolds Number Second Moment Closure

In second approach, the low Reynolds number second moment closure of Memon, [15], which is based on the suggestions of Lai and So, [16] has been adopted for the predictions. In this modelling procedure, an isotropic eddy viscosity approach is not invoked and the transport equations in the near wall region are resolved for each Reynolds stress component, called Reynolds stress closure. The governing equations for the Reynolds stress tensor can be expressed in Cartesian tensor as:

$$\frac{\partial}{\partial x_k}\left(\rho U_k \overline{u_i u_j}\right) = \frac{\partial}{\partial x_k}\left(\mu \frac{\partial \overline{u_i u_j}}{\partial x_k}\right) + \frac{\partial}{\partial x_k}\left(-\rho \overline{u_i u_j u_k}\right) - \rho\left(\overline{u_j u_k}\frac{\partial U_i}{\partial x_k} + \overline{u_i u_k}\frac{\partial U_j}{\partial x_k}\right) - \overline{\left(u_i \frac{\partial p}{\partial x_j} + u_j \frac{\partial p}{\partial x_i}\right)} - 2\mu \overline{\frac{\partial u_i}{\partial x_k}\frac{\partial u_j}{\partial x_k}} \quad (7)$$

or symbolically as:

$$C_{ij} = D_{ij}^{\nu} + D_{ij}^{T} + P_{ij} + \Pi_{ij} - \varepsilon_{ij} \quad (8)$$

where from left to the right can be read as convection, viscous diffusion, turbulent diffusion, production by mean strain, redistribution and diffusion due to the pressure interactions and viscous dissipation of the Reynolds stresses respectively.

Modelling of the turbulent diffusion, pressure-strain interactions and viscous dissipation terms individually formed the exact equation for the low Reynolds number second moment closure, which represents the all the correlations in detail given as under:

$$\begin{aligned} C_{ij} = {} & \frac{\partial}{\partial x_k}\left[\mu \frac{\partial \overline{u_i u_j}}{\partial x_k}\right] + \frac{\partial}{\partial x_k}\left[\rho c_s \frac{k}{\varepsilon}\overline{u_k u_l}\frac{\partial \overline{u_i u_j}}{\partial x_l}\right] - \\ & \rho\left[\overline{u_j u_k}\frac{\partial U_i}{\partial x_k} + \overline{u_i u_k}\frac{\partial U_i}{\partial x_k}\right] \\ & - \rho c_1 \frac{\varepsilon}{k}\left[\overline{u_i u_j} - 2/3\delta_{ij}k\right] - c_2\left[P_{ij} - 2/3\delta_{ij}P_k\right] \\ & + f_w\left[\rho c_1 \frac{\varepsilon}{k}\left(\overline{u_i u_j} - 2/3\delta_{ij}k\right) + \alpha\left(P_{ij} - 2/3\delta_{ij}P_k\right) - \rho\frac{\varepsilon}{k}\left(\overline{u_i u_k}n_k n_j + \overline{u_j u_k}n_k n_i\right)\right] \\ & - 2/3\delta_{ij}\rho\varepsilon\left(1 - f_w\right) - f_w\rho\frac{\varepsilon}{k}\frac{\left(\overline{u_i u_j} + \overline{u_i u_k}n_k n_j + \overline{u_j u_k}n_k n_i + n_i n_j \overline{u_k u_l}n_k n_l\right)}{1 + 3\overline{u_k u_l}n_k n_l/2k} - \frac{\overline{u_i u_j}}{k}D_k \end{aligned} \quad (9)$$

For full details of these terms, refer Memon, [15] and Lai and So [16].

4. COMPUTATIONAL PROCEDURE

Isothermal predictions are conducted by adopting the TEACH computational procedure of Gosman and Ideriah [17] , which uses a Finite Volume Method and adopts the line-by-line method based on the TDMA (Tri Diagonal Matrix Algorithm) to solve the discretized transport equations. All variables available in the transport equations are calculated at the main grid nodes, whereas the momentum equations in axial and radial directions are solved by the staggered grid arrangement of Harlow and Welch [18], as shown in Fig. 2. A finite-difference technique of Patankar [19] is employed for a Steady-state solution in the axisymmetric cylindrical polar co-ordinate frame of reference. To maintain the mass continuity and couple the pressure-velocity flow field, the SIMPLEC (Semi-Implicit Method for Pressure Linked Equations) algorithm of Van Doormal and Raithby [20] has been employed. A non-uniform grid composed of 75x92 nodes in the axial and radial directions respectively has been adopted as shown in Fig. 3. During the transformation process, the unknown values of the variable appeared in the algebraic equations are required to be discretised at finite number of grid points of the calculating domain. Therefore, to evaluate the unknown variables at the control volume faces, the HYBRID, Spalding [21], and HOUS (High Order Upwind Scheme), Castro and Jones, [22] discretisation schemes have been adopted in combined form for the mean and fluctuating components respectively. This combination was found reliable and economical by Memon [15] and Morse [12] for their computational work.

5. DISCUSSION OF NUMERICAL RESULTS

This section presents the predicted results for the flow structure, mean velocity profiles and computed moment

coefficient for a rotating cavity system with radial outflow condition.

5.1 Computed Flow Structure

Fig. 4(i-iv) show computed flow structures in the r-z plane for the rotational Reynolds numbers of the range $1x10^5 \leq Re_\theta \leq 4x10^5$ and two different mass flow rates C_w=(1092 and 2184). Computed flow structures illustrated the four flow regions: source, Ekman layers, an interior core and sink. These computed flow regions show the consistency with the previous experimental and numerical work of Owen, et. al. [3], Pincombe, [11], Schiestel, et. al. [4], Memon [23], Kilic, et. al. [24] and Javiya, et. al. [25].These flow structures illustrated that the incoming cooling air enters the cavity axially through a central hole in the left hand disc (upstream disc), impinges on the right hand disc (downstream disc) and forms a wall jet on this disc in radial direction. The wall jet extended in the source region up to the radius $r<r_e$, where r_e is the radial extension of the source. Before entraining the boundary layer of the left hand (upstream) disc, the fluid recirculated in the vicinity of the source region and forms a recirculating zone, where radial and axial velocity components became zero. After the source region, the fluid flows along both discs and forms Ekman boundary layers and redistributed to the sink region then leaves the cavity through a hole in the outer shroud. For the lowest value of the rotational Reynolds number $Re_\theta=1x10^5$ and low mass flow rate, a strong wall-jet and large recirculation zone is formed in the vicinity of the source region, as shown in Fig. 4(i), which effect the entire flow structure in the cavity. For a 100% higher rotational Reynolds number, $Re_\theta=2x10^5$ and the same mass flow rate, the size of the wall-jet and the recirculation core are decreased as shown in Fig. 4(ii), consequently the earlier entraining boundary layers are formed on both discs. Further increase in the rotational Reynolds number, $Re_\theta=4x10^5$ for the same mass flow rate, the significant effects are obvious on the flow structure particularly, on wall-jet and the size source region and subsequently the strength of the recirculation zone in this region, which results in the earlier development of entraining boundary layers on both the discs, as shown in Fig. 4(iii). For a lower value of rotational Reynolds number, $Re_\theta=1x10^5$ and 100%

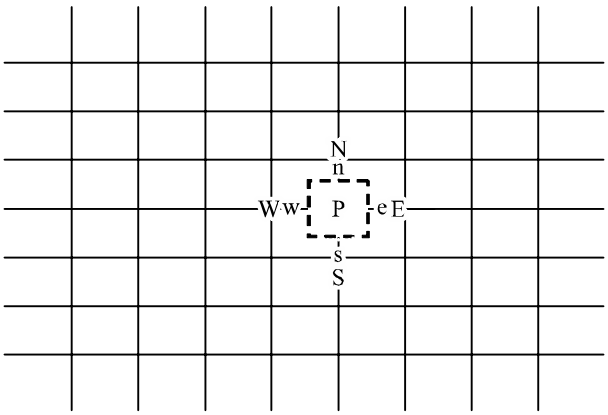

FIG 2. STAGGERED GRID ARRANGEMENTS

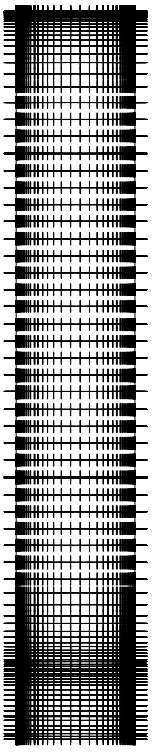

FIG. 3. NON-UNIFORM GRID

higher mass flow rate, C_w=2184, the incoming fluid impinged on the downstream disc and extended the size and strength of the vortex within the source region. Consequently the strong wall-jet is formed along the downstream disc. This recirculating core dominated the flow structure entire cavity and major portion of the fluid from entraining boundary layer is redistributed in the sink layer, as shown in Fig. 4(iv).

5.2 Computed Velocity Profiles

Fig. 5(i-iii) show a comparison of the two turbulence models for the computed radial velocity profiles for the rotational Reynolds numbers of the range $1x10^5 \leq Re_\theta \leq 4x10^5$ and two different mass flow rates C_w=(1092 and 2184). In first case the value of mass flow rate C_w=1092 is fixed to examine the influence of the rotational Reynolds number, through considering three values rotational Reynolds number $Re_\theta=1x10^5$, $Re_\theta=2x10^5$ and $Re_\theta=4x10^5$. For these Reynolds numbers the peak of boundary layer is increased monotonically and reached at maximum level at higher Reynolds number. Comparison of two models for radial location r/b=0.633 and 0.833 show that the low Reynolds number k-ε model overestimates the peak of boundary layer on the upstream disc, whereas the low Reynolds number second moment closure predictions show a good level of agreement with the experimental data at lower radial location r/b=0.633. For higher radial location, r/b= 0.833, the level of velocity profile increased to 58% than the previous lower radial location. A comparison of two models shows that the low Reynolds number k-ε model slightly overestimated the upstream disc whereas the low Reynolds number second moment closure is more accurate in this region. A closer agreement of the low Reynolds number second moment closure reveals that in account of enhance wall treatment put the significant effects on the predictions and enables the model to estimate the correct anisotropic behaviour of the flow in the near wall region. Because in this region viscous effects are more dominant than those are in the central region. Schiestel, et. al. [4] mentioned that the near-wall description is crucial for obtaining the realistic flow behaviour than that of the fully turbulent region.

Fig. 5(iv) illustrates the comparison of predictions for a 100% higher mass flow rate C_w=2184 and lower rotational Reynolds number $Re_\theta=1x10^5$. For this highest value of

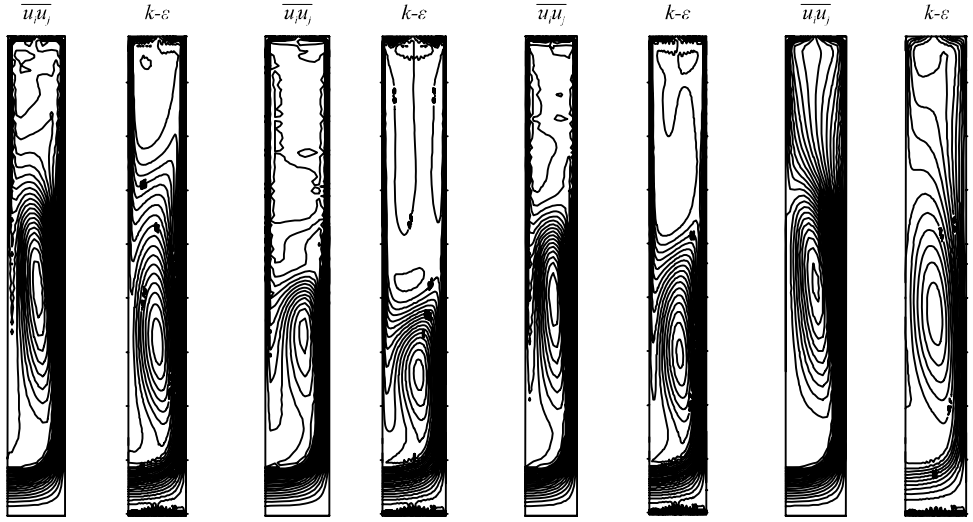

(i) Re_O =1x10^5 , C_w=1092 (ii) Re_O = 2x10^5, C_w=1092 (iii) Re_O = 4x10^5 , C_w=1092 (iv) Re_O =1x10^5, C_w = 2184

FIG. 4. COMPUTED STREAMLINES FOR COROTATING DISC FLOW SYSTEM

the mass flow rate, the experimental data is not available for lower radial location (i.e. r/b=0.633), thus comparison of radial velocity component is presented only for the higher radial location (i.e. r/b=0.833). A comparison of two models show that both the models predicted a 60% lower peak of the boundary layer than that of first case of a lower mass flow rate. This decrease in the boundary layer peak revealed the significant effects of a mass flow rate. The low Reynolds number k-ε model predicted lower peak of boundary layer than the experimental data. However, the low Reynolds number second moment closure produced a higher peak and thicker boundary layer and shows a closer agreement with measurements than that of the k-ε model.

Fig. 6(i-iv) presents the comparison of computed tangential velocity profiles for a range of rotational Reynolds numbers, $1x105 \leq Re_\theta \leq 4x10^5$ and fixed value of mass flow rate C_w=1092. The comparison of two models at lower rotational speed shows the larger vortex and higher peak of tangential velocity profile in the source region. The low Reynolds number second moment closure predicted the slightly higher peak than that of the low Reynolds number k-ε model. This trend of higher peak of tangential velocity profile shows the consistency with the computed flow structure for the same flow conditions (Fig. 4 i-ii).

The comparison of the two models with the measurements of Pincombe [11] showed that at a lower rotational speed, both models underestimate the experimental data; however the k-ε model shows slightly better agreement with the measurements, as shown in Fig. 6(i-ii). For highest rotational Reynolds number, $Re_\theta=4x10^5$ and the same flow rate, the source region flow is further contracted and Ekman layers are formed on both discs at earlier stage of the cavity, which resulted in 75% decrease in the peak of tangential velocity profile, as shown in Fig. 6(iii). A comparison of the two models with the measurement illustrates that the low Reynolds number second moment closure shows a good agreement with the experimental data than that of the k-ε model. For a 100% higher mass flow rate C_w=2184 and lower rotational Reynolds number $Re_\theta=1x10^5$, a comparison of two models shows the significant differences in the predicted tangential velocity profiles. Both the models show the noticeable variations in the source region as well as in the outer part of the cavity, as shown in Fig. 6(iv). These variations reveal the effects of higher mass flow rate on the flow behaviour and formed larger recirculating vortices (eddies) in the source region. However, both the models showed a closer agreement with the available data points of Pincombe [11] in the outer part of the cavity.

5.3 Computed Moment Coefficient

Further assessment of the two turbulence models are carried out through the comparison of predicted variation of the moment coefficients (C_m) for the range of rotational Reynolds number $1x10^5 \leq Re_\theta \leq 4x10^5$ and mass flow rates, C_w=1092 and 2184 as shown in Table 1. Unfortunately for this typical case of the rotating cavity flows, the experimental data for the moment coefficient is not available for validation purpose. Therefore, a comparison of the two models has been carried out by considering the parametric effects. The general trend of variation in the computed moment coefficient of two models indicated that for the higher rotational speed the moment coefficient decreased on both discs. Whereas, for a higher mass flow rate, the value of the moment coefficients on both discs increased, particularly on downstream disc, which reveals the strong wall jet effect on this disc and the tendency of the flow symmetry on both the discs. The same trends of variation in the computed moment coefficient for varying rotational speeds were noted in the computational work of Morse [26] and Memon [15] and Abbasi, et. al. [27].

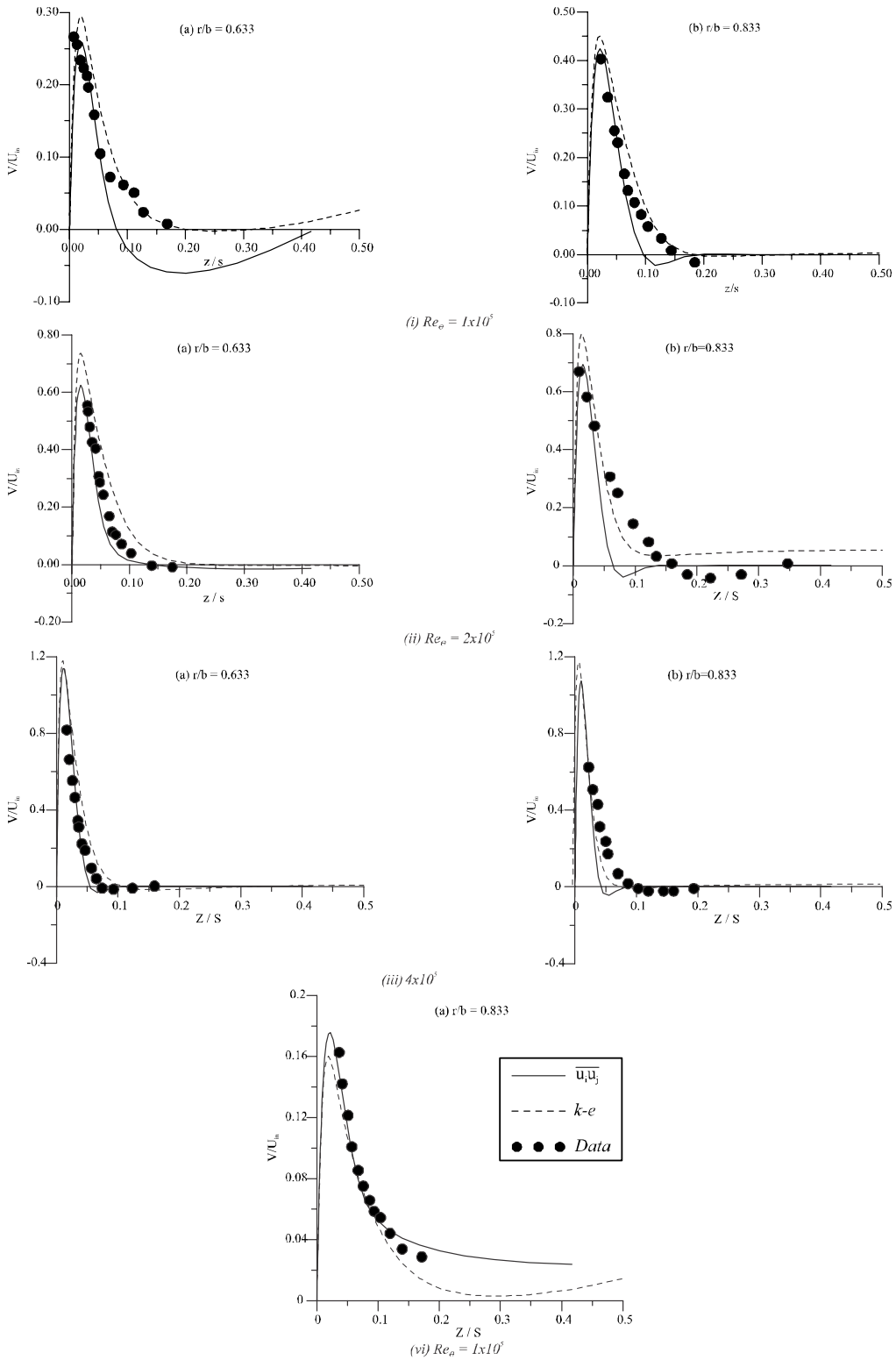

FIG. 5. COMPARISON BETWEEN THE COMPUTED AND MEASURED RADIAL VELOCITY PROFILE FOR TWO VALUES OF C_w=1092 AND C_w=2184

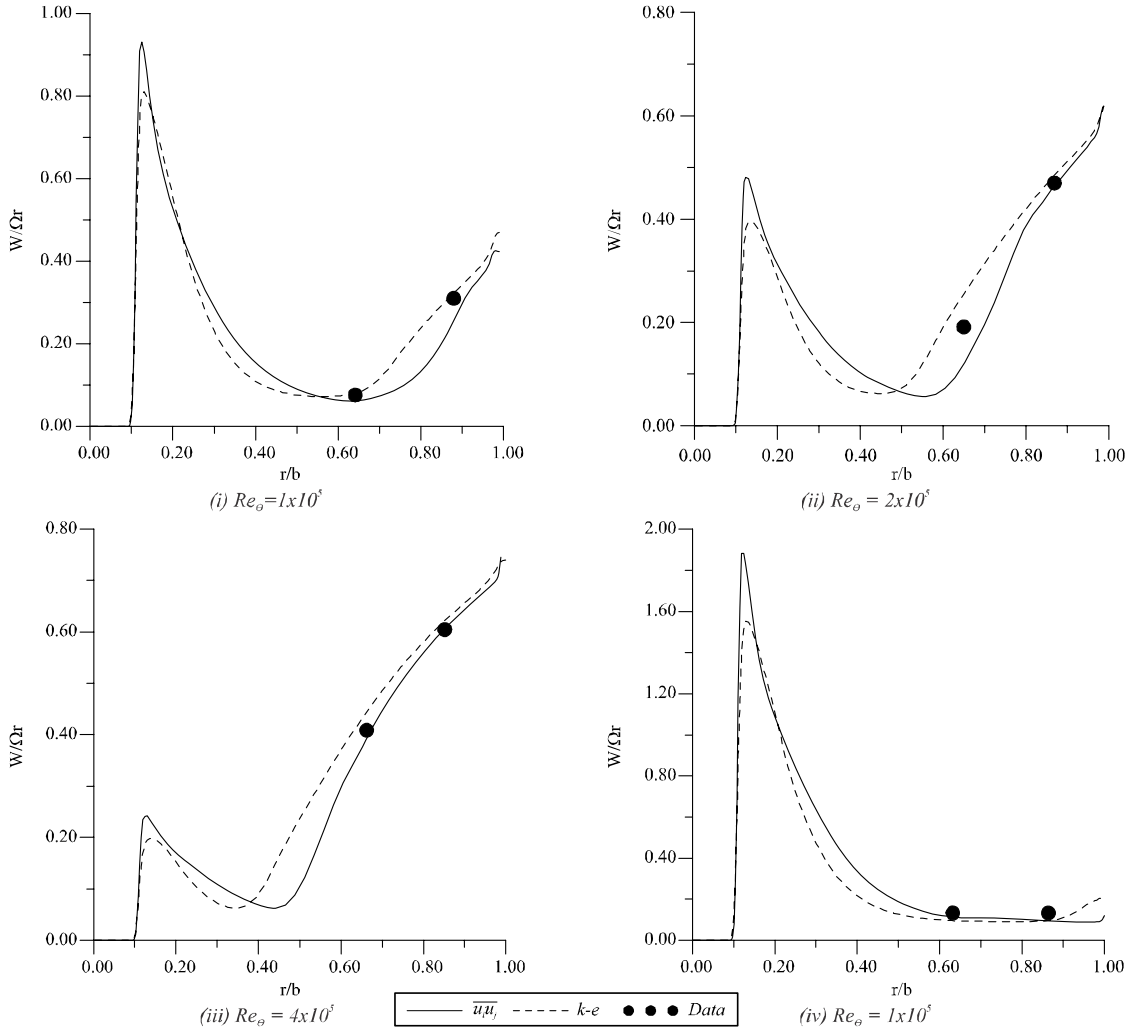

FIG. 6. COMPARISON BETWEEN THE COMPUTED AND MEASURED TANGENTIAL VELOCITY PROFILES FOR TWO VALUES OF C_w=1092 AND C_w=2184

TABLE 1. COMPARISON BETWEEN COMPUTED MOMENT COEFFICIENTS

Re_θ	C_w	Up-Stream Disc (C_mx10^3)		Down-Stream Disc (C_mx10^3)	
		k-ε	$\overline{u_i u_j}$	k-ε	$\overline{u_i u_j}$
1x10^5	1092	5.62	5.63	6.11	6.13
2x10^5	1092	3.56	3.57	3.68	3.76
4x10^5	1092	2.02	2.05	2.05	2.16
1x10^5	2184	6.34	6.51	7.50	7.58

6. CONCLUSIONS

Isothermal rotating cavity flow system was investigated for the range of low to moderate Reynolds number and two mass flow rates. In previous studies the rotating cavity flows at lower operating conditions was invesigated using of two turbulence models. In this research, the comparative model based study is carried out at low to moderate operating conditions. The comparison of two models, the k-ε model and low Reynolds number second moment closure model showed the model-dependent behaviour of

rotating disc cavity system, particularly in recirculation and impingement regions where flow was more turbulent. Computed flow structures showed that the radial extension of the source region was significantly affected by the strength of recirculating vortices (eddies). These vortices increase with either increase in the mass flow rate or decrease in the rotational Reynolds number. The comparison of the radial velocity profiles showed that for the higher rotational Reynolds number, the low Reynolds number second moment closure predicted higher peaks of the velocity profiles than that of the k-ε model and showed a good agreement with the measurements. Further, assessment of the models was carried out for the predicted moment coefficients. The general trends of variation in the computed moment coefficients showed that for a fixed value of mass flow rate and varying rotational speeds, the values of those coefficients for both discs decreased. This revealed the trend of the flow symmetry for both discs. However, the increase in mass flow rate for a lower Reynolds number resulted in higher moment coefficient. Overall comparison of two models concluded that for higher flow conditions, the low Reynolds number second moment closure showed its robustness over the k-ε model. Therefore, the low Reynolds number second moment closure model can be used for more complex geometries of practical interest, particularly gas turbine engines and compressor disc spaces. For future work, it is recommended that the experimental data for higher operating conditions ($Re_\theta > 10^6$) be obtained to check the validity of the low Reynolds number second moment closure.

7. NOMENCLATURE

b	outer radius of cavity
$C_w = \dot{m}/\mu b$	non-dimensional mass flow rate
$C_m = M/\frac{1}{2}\rho\Omega^2 b^5$	moment coefficient
$G=s/b$	cavity gap ratio
k	turbulent kinetic energy
M	frictional moment
$Re_\theta=\Omega b^2/\nu$	rotational Reynolds number
r	radial coordinate
r/b	non-dimensional radial coordinate
r_i	inner disc radius
S	source term
s	axial gap between the discs
S_c	clearance between shrouds
U,V,W	mean velocity components in z, r, θ
U_i	axial inlet velocity
V_o	radial outlet velocity
u,v,w	fluctuating velocity components in z, r, θ
$\overline{u_i u_j}$	Reynolds stress tensor
z	axial coordinate
z/s	non-dimensional axial coordinate
ε	dissipation rate of turbulent kinetic energy
ν	kinematic viscosity
μ	dynamic viscosity
μ_T	turbulent viscosity
ϕ	generalised transport variable
Ω	rotational speed of the discs
ρ	density
δ_{ij}	Kronecker delta
f_w	near-wall function for Reynolds stress equation
α	coefficient of wall reflection term in $\overline{u_i u_j}$

ACKNOWLEDGEMENTS

Authors are also thankful to the MUET (Mehran University of Engineering & Technology), and Faculty Members, Department of Mechanical Engineering, MUET, Jamshoro, Pakistan, for their encouragement and moral support. The second author would like to acknowledge the Higher Education Commission, Ministry of Science & Technology, Government of Pakistan, for providing financial support to complete Ph.D. work.

REFERENCES

[1] Childs, P.R.N., Dullenkopf, K., and Bohn, D., "Internal Air Systems Experimental Rig Best Practice", ASME Paper GT2006-90215, 2006.

[2] Owen, J.M., "Thermodynamic Analysis of Buoyancy-Induced Flow in Rotating Cavities", Journal of Turbomachinery, Volume 132, pp. 031006-1-031006-7, 2010.

[3] Owen, J.M., "Prediction of Ingestion through Turbine Rim Seals Part-I: Rotationally Induced Ingress", Journal of Turbomachinery, Volume 133, pp. 031005-1-031005-9, 2011.

[4] Schiestel, R., Elena, L., and Rezoug, T., "Numerical Modelling of Turbulent Flow and Heat Transfer in Rotating Cavities", Numerical Heat Transfer, Part-A Applications, Volume 24, pp. 45-55, 1993.

[5] Owen, J.M., and Rogers, R.H., "Rotating Cavities, Flow and Heat Transfer in Rotating Disc Systems", Rotating Cavities, Volume 2, Research Studies Press, John Wiley Inc., New York, 1995.

[6] Gan, X., Mirzaee, I., Owen, J.M., Rees, D.A.S., and Wilson, M., "Flow in a Rotating Cavity with a Peripheral Inlet and Outlet of Cooling Air", International ASME Gas Turbine and Aeroengine Congress, Paper 96-GT-309, Birmingham, 1996.

[7] Soong, C.Y., Wu, C.C., and Liu, T.P., "Flow Structure between Two Co-Axial Discs Rotating Independently", Experimental Thermal and Fluid Science, Volume 27, pp. 295311, 2003.

[8] Randriamampianina, A., Schiestel, R., and Wilson, M., "The Turbulent Flow in an Enclosed Corotating Disk Pair: Axisymmetric Numerical Simulation and Reynolds Stress Modeling", International Journal of Heat and Fluid Flow, Volume 25, pp. 897-914, 2004.

[9] Poncet, S., DaSoghe, R., and Facchini, A., "RANS Modelling of Flow in Rotating Cavity System", 5th European Conference on Computational Fluid Dynamics, Lisbon, Portugal, 2010.

[10] Owen, J.M., and Pincombe, J.R., "Velocity Measurements Inside a Rotating Cylindrical Cavity with a Radial Outflow of Fluid", Journal of Fluid Mechanics, Volume 99, No. 1, pp. 111-127, 1980.

[11] Pincombe, J.R., "Optical Measurements of the Flow Inside a Rotating Cylinder", Ph.D. Thesis, University of Sussex, 1983.

[12] Morse, A.P., "Application of a Low Reynolds Number k-ε Turbulence Model to High-Speed Rotating Cavity Flows", Journal of Turbomachinery, Volume 113, pp. 98-105, 1991.

[13] Jones, W.P., and Launder, B.E., "The Prediction of Laminarization with a Two-Equation Model of Turbulence", International Journal of Heat and Mass Transfer, Volume 15, pp. 301-314, 1972.

[14] Jones, W.P., and Launder, B.E., "The Calculation of Low Reynolds Number Phenomena with a Two-Equation Model of Turbulence", International Journal of Heat and Mass Transfer, Volume 16, pp. 1119-1130, 1973.

[15] Memon, M.D., "Numerical Modelling and Prediction of Fluid Flow and Heat Transfer in Rotating Disc Geometries", Ph.D. Thesis, University of Sussex, 1995.

[16] Lai, Y.G., and So, R.M.C., "On Near-Wall Turbulent Flow Modelling", Journal of Fluid Mechanics, Volume 221, pp. 641-673, 1990.

[17] Gosman, A.D., and Ideriah, F.J.K., "TEACH-T: A General Computer Program for Two-Dimensional Turbulent Recirculating Flows'. See "Calculation of Recirculating Flows", Deptartment of Mechanical Engineering, Imperial College, University of London, 1976.

[18] Harlow, F.H., and Welch, J.E., "Numerical Calculation of Time-Dependent Viscous Incompressible Flow of Fluid with Free Surface", Physics of Fluids, Volume 8, pp. 2182-2189, 1965.

[19] Patankar, S.V., "Numerical Heat Transfer and Fluid Flow", McGraw-Hill, New York, 1980.

[20] Van Doormal, J.P., and Raithby, G.D., "Enhancement of the SIMPLE Method for Predicting Incompressible Fluid Flow", Numerical Heat Transfer, Volume 7, pp. 147-163, 1984.

[21] Spalding, D.B., "A Novel Finite-Difference Formulation for Differential Expression Involving Both First and Second Derivatives", International Journal of Numerical Methods Engineering, Volume 4, pp. 551-567, 1972.

[22] Castro, I.P., and Jones, J.M., 'Studies in Numerical Computations of Recirculating Flows", International Journal of Numerical Methods in Fluids, Volume 7, pp. 793-810, 1987.

[23] Memon, M.D., and Uqaili, M.A., "Computation of Fluid Flow and Heat Transfer in Sealed Rotating Cavity", Mehran University Research Journal of Engineering & Technology, Volume 21, No. 2, pp. 97-108, Jamshoro, Pakistan, April, 2002.

[24] Kilic, M., and Owen, J.M., "Computation of Flow between Two Discs Rotating at Different Speeds", Journal of Turbomachinery, Volume 125, pp. 394-400, 2003.

[25] Javiya, U., Chew, J.W., Hills, N.J., Zhou, L., Wilson, M., and Lock, G.D., "CFD Analysis of Flow and Heat Transfer in a Direct Transfer Preswirl System", Journal of Turbomachinery, Volume 134, pp. 031017-1, 2012.

[26] Morse, A.P., "Numerical Prediction of Turbulent Flow in Rotating Cavities", Journal of Turbomachinery, Volume 110, pp. 202-211, 1988.

[27] Abbasi, A.F., Memon, M.D., and Baloch, A., "Modelling and Predictions of Isothermal Flow Inside the Closed Rotor-Stator Flows", Mehran University Research Journal of Engineering & Technology, Volume 31, No. 1, pp. 83-94, Jamshoro, Pakistan, January, 2012.